MATERIALS SCIENCE

High-*k* perovskite gate oxide for modulation beyond 10^{14} cm^{-2}

Dowon Song[1], Myoungho Jeong[2], Juhan Kim[1], Bongju Kim[1], Jae Ha Kim[3], Jae Hoon Kim[3], Kiyoung Lee[2], Yongsung Kim[2], Kookrin Char[1]*

Copyright © 2022 The Authors, some rights reserved; exclusive licensee American Association for the Advancement of Science. No claim to original U.S. Government Works. Distributed under a Creative Commons Attribution NonCommercial License 4.0 (CC BY-NC).

Scaling down of semiconductor devices requires high-*k* dielectric materials to continue lowering the operating voltage of field-effect transistors (FETs) and storing sufficient charge on a smaller area. Here, we investigate the dielectric properties of epitaxial $BaHf_{0.6}Ti_{0.4}O_3$ (BHTO), an alloy of perovskite oxide barium hafnate ($BaHfO_3$) and barium titanate ($BaTiO_3$). We found the dielectric constant, the breakdown field, and the leakage current to be 150, 5.0 megavolts per centimeter (MV cm^{-1}), and 10^{-4} amperes per square centimeter at 2 MV cm^{-1}, respectively. The results suggest that two-dimensional (2D) carrier density of more than $n_{2D} = 10^{14}$ per square centimeter (cm^{-2}) could be modulated by the BHTO gate oxide. We demonstrate an n-type accumulation mode FET and direct suppression of more than $n_{2D} = 10^{14}$ cm^{-2} via an n-type depletion-mode FET. We attribute the large dielectric constant, high breakdown field, and low leakage current of BHTO to the nanometer scale stoichiometric modulation of hafnium and titanium.

INTRODUCTION

Over the past several decades, Si-based device technology has been relentlessly scaled down. To reduce thermal heating and power consumption, lowering operating voltage is required, which can be resolved through higher capacitance. This has been leading to thinner gate oxide as the devices shrink in size. However, reduced thickness of the gate oxide results in increased leakage current via direct tunneling, which limits the device performance. For overcoming these limitations, high-*k* materials have been investigated to attain equivalent capacitance with thicker gate oxide thickness (*1*–*5*). High-*k* dielectrics require the following two properties: high dielectric constant and high dielectric strength under high electric field.

Recently, in the field of iontronics, electric double layer transistors (EDLTs) are generating a substantial impact, since the electric field at the EDL interface is on the order of 10 MV cm^{-1}, and the accumulated carrier density can be on the order of 10^{14} cm^{-2} (*6*). Charge accumulation capability in a ZnO field-effect transistor (FET) gated by EDLs of ionic liquid reached an ultrahigh carrier density of 8×10^{14} cm^{-2} at 220 K (*7*). In addition, EDLT on a high-mobility semiconducting perovskite $BaSnO_3$ channel was reported, which modulated the carrier density over 10^{14} cm^{-2} (*8*). EDLTs are fascinating subjects for scientific investigation; however, the "liquid" nature of EDLTs is a strong challenge for their use in practical devices. Furthermore, the capacitance of ionic liquid diminishes rapidly by a factor of 10^4 between the frequency of 10^{-2} and 10^4 Hz due to the fundamentally sluggish motion of mobile ions, which hinders its use for device applications in addition to electrochemical reaction (*6*, *7*).

Unfortunately, materials with high dielectric constant usually exhibit weak dielectric strength; the breakdown field is low and/or their leakage current is large in high electric field (*5*, *9*–*11*). When an external electric field is applied to a high-*k* dielectric layer, a large Lorentz local field, given by $E_{loc} = \left(\frac{k+2}{3}\right)E_{ext}$, is applied to high-*k* materials. This large Lorentz local field results in bond breaking, generating defects, and forming conductive percolation path, followed by dielectric breakdown (*5*). However, extrinsic defects often determine the material's breakdown field before intrinsic breakdown occurs. Therefore, the actual breakdown field of material could be accompanied by extrinsic defects, resulting in varying breakdown field even in the same material. In effect, materials with high dielectric constants have weak dielectric strength due to their narrow bandgap and vulnerability to ionic displacement (*5*, *12*). Therefore, finding the materials with both high dielectric constant and high dielectric strength is quite challenging but important.

Two classes of high-*k* perovskite oxides have been evaluated in the past by growing them epitaxially on Si (*13*–*18*). The class of titanates, (Ba or Sr)TiO_3, has been most studied because of their high dielectric constant of a few hundreds, but the prior demonstrations had limited impact because of the high leakage currents. On the other hand, using hafnates, particularly $SrHfO_3$, an FET on silicon is successfully fabricated down to an equivalent oxide thickness (EOT) of 1.2 nm (*17*). However, because of its moderate dielectric constant (~30), scaling below an EOT of 1 nm was challenging.

Combination of distinct solid-state systems frequently introduces wholly new functionality or enhanced properties through modulating degree of freedoms such as epitaxial strain, charge, and spin. In addition, even with identical composition, different configurations of each atom could result in dissimilar material properties. Artificial superlattice is the one of the prominent exemplifications, and supercrystal phases were reported in composite ferroelectrics $K_{1-\alpha}Li_{\alpha}Ta_{1-\beta}Nb_{\beta}O_3$ (KLTN) (*19*) and $PbTiO_3/SrTiO_3$ superlattice (*20*) and $PbTiO_3/SrRuO_3$ superlattice (*21*). Furthermore, the mechanism for the enhanced piezoelectricity in multielement-doped (K,Na)NbO_3 ceramics was reported recently (*22*). Motivated by these prior works, we investigated $BaHfO_3$ (BHO)/$BaTiO_3$ (BTO) composite system to examine how the system builds specific microstructure and its material properties, especially its dielectric properties.

Recently, BHO is reported to have relatively high dielectric constant and low leakage current and used successfully as a gate oxide (*23*). Ferroelectricity in BTO, a well-known ferroelectric perovskite, is

[1]Institute of Applied Physics, Department of Physics and Astronomy, Seoul National University, Seoul 08826, Republic of Korea. [2]Samsung Advanced Institute of Technology (SAIT), Samsung Electronics Co. Ltd., Suwon 16678, Republic of Korea. [3]Department of Physics, Yonsei University, Seoul 03722, Republic of Korea.
*Corresponding author. Email: kchar@snu.ac.kr

accounted for by the titanium atomic displacement in TiO_6 octahedra, and these ferroelectric materials are highly polarizable in an external field, which correlates with its high leakage current (*24*). The room temperature dielectric constant of BTO ceramics can be greater than 2000. However, its dielectric constant in thin film forms is much lower, ranging between 200 and 400 (*25*). Although high breakdown field in amorphous BTO films has been reported earlier (*26*), its dielectric constant was only 16. Furthermore, the breakdown field of crystalline BTO thin film is about 1 MV cm^{-1}, which limits the application of the material (*27*). By alloying these two materials, one may achieve both the high dielectric constant of BTO and the high dielectric strength of BHO. There have been a few reports that investigated $BaHf_{1-x}Ti_xO_3$ system, but no detailed dielectric properties were reported (*28–32*). Here, we report a high-*k* material with superior dielectric properties: large dielectric constant (~150) and high breakdown field (~5 MV cm^{-1}) with low leakage current (~10^{-4} A cm^{-2} at 2 MV cm^{-1}). Using such BHTO, large carrier density on the order of 10^{14} cm^{-2} can be completely modulated.

RESULTS AND DISCUSSION

Electrical properties

To measure the electrical properties of $BaHf_{0.6}Ti_{0.4}O_3$ dielectric, degenerately doped 4% La-doped $BaSnO_3$ (4% BLSO of ~150 nm in thickness and 150-microhm·cm resistivity) (*33*) was epitaxially grown as the top electrode on 200-nm-thick $BaHf_{0.6}Ti_{0.4}O_3$ in a mesa-like capacitor structure with 4% BLSO bottom electrode. The thickness of BHTO has been confirmed by Kiessig fringes of x-ray diffraction in fig. S1 and table S1. The area of the top 4% La-doped $BaSnO_3$ electrode is about 53,100 μm^2 (diameter of ~260 μm). From the measured parallel capacitance (C_p), the dielectric constants (*k*) of $BaHf_{0.6}Ti_{0.4}O_3$ were calculated. Capacitance-frequency and current-voltage characteristics are shown in Fig. 1 (A and B). The DC field dependence of the capacitance is in Fig. 1C. The DC field dependence looks similar to those based on BTO or $SrTiO_3$ (*28*, *34*). This DC field dependence of the dielectric constant in titanates is related with the hardening of the soft phonons (*35*, *36*). Because of the large bias dependence of the dielectric constant, the "effective" dielectric constant in a device will be reduced, being the average dielectric constant in the range of zero to a finite bias. Multifrequency and double-sweep capacitance-voltage (*C*-*V*) measurements are in fig. S2. In addition, the band offset estimation by Fowler-Nordheim tunneling analysis of the leakage current at high bias and the corresponding band diagrams are in fig. S3.

To obtain the statistics of the dielectric constant and the breakdown field of the $BaHf_{0.6}Ti_{0.4}O_3$ dielectric, we fabricated 21 (3 × 7) capacitors on a single chip and collected their electrical properties in fig. S4. The statistically averaged dielectric constant of $BaHf_{0.6}Ti_{0.4}O_3$ is about 150, and most of the dielectric constants are in the range of 145 to 155, which is larger than twice the reported value of 65 (*30*). Theoretical dielectric constants can be calculated by effective medium theories. A few exemplary calculations are listed in table S2, where ε_{BHTO}, ε_{BHO}, and ε_{BTO} are dielectric constants of $BaHf_{1-x}Ti_xO_3$, BHO, and BTO, respectively, and f_{BHO} and f_{BTO} are volume fractions of BHO and BTO, respectively, which correspond to 0.6 and 0.4. In classical effective medium theory, considering the reported dielectric constant of BHO and BTO, which is 37.8 and 200 to 600, the effective medium theory generates 56.6 to 61.5 for dielectric constants of $BaHf_{0.6}Ti_{0.4}O_3$, which is much lower than our experimental values. Even if we use the high dielectric constant (~4000) of single-crystal BTO, the calculated value of 63.9 is not much different. Even in Maxwell-Garnett approximation, which assumes embedded solid nanospheres in a host material, calculated dielectric constant of BHTO falls short of experimental values at any case of BTO dielectric constant, probably due to the limitation of the model that validates only when the volume fraction of nanospheres is relatively low (<0.1). However, in the framework of Bruggeman approximation, of which host and guest materials are indistinguishable and the system is completely random, calculated dielectric constant predicts the experimental dielectric constant of 150 when assuming the dielectric constant of BTO as 600. Statistically averaged breakdown field is 3.2 MV cm^{-1}, and its deviation is much larger than that of the dielectric constant. This result can be attributed to the fact that the dielectric breakdown depends more on the local defects in each capacitor. Thus, in the case of breakdown

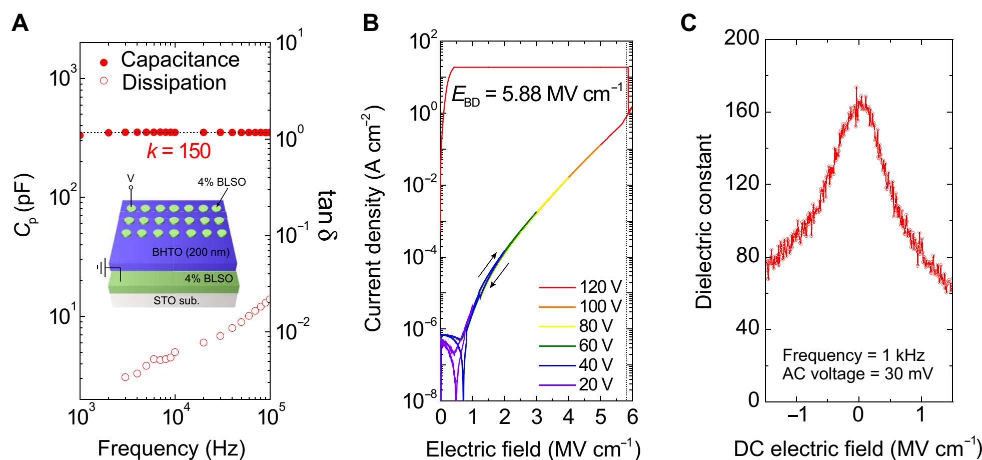

Fig. 1. Dielectric properties of BHTO. (**A**) Frequency-dependent capacitance curve of a $BaHf_{0.6}Ti_{0.4}O_3$ metal-insulator-metal device. The inset shows the layer structure of the device. STO, $SrTiO_3$. (**B**) Leakage current density as a function of electric field of the $BaHf_{0.6}Ti_{0.4}O_3$ device in (A). (**C**) Electric field dependence of dielectric constant measured at 1 kHz with an AC bias of 30 mV.

field, the maximum value, rather than the average value, of the measured breakdown field will better represent the intrinsic dielectric strength. A few capacitors exhibited dielectric breakdown field larger than 5.0 MV cm^{-1}. Some representative current density–electric field characteristics are shown in the fig. S5. From these dielectric properties of $BaHf_{0.6}Ti_{0.4}O_3$, calculated maximum field-induced charge density is beyond 10^{14} cm^{-2} at 2 MV cm^{-1}, of which the leakage current density is 10^{-4} A cm^{-2}, which corresponds to a leakage current of 10^{-12} A in a 1-μm^2 size device. Even considering the DC field dependence of the dielectric, field-induced charge density is larger than 10^{14} cm^{-2}.

Figure 2 shows comparison among dielectric materials with their dielectric constants and breakdown fields. More data on various binary and ternary dielectrics are listed in table S3. The experimental data are from the paper by McPherson *et al.* (*5*). We plotted the maximum two-dimensional (2D) charge density curve that can be modulated by dielectrics, which is proportional to the product of dielectric constant and breakdown field. We also plotted the theoretical and experimental curve by McPherson model (*10*), which is given by $E_{BD} = 35.3\ (k)^{-0.64}$ and $E_{BD} = 29.9\ (k)^{-0.65}$ (theoretical and experimental, respectively). From the electrical measurement, the dielectric constant of $BaHf_{0.6}Ti_{0.4}O_3$ dielectric is about 150, and the corresponding breakdown field is about 5 MV cm^{-1}, which results in the maximum field-induced charge density of about 4×10^{14} cm^{-2}, although the maximum electric field in devices is usually limited by the leakage current constraint depending on the device geometry. Nevertheless, the values of $BaHf_{0.6}Ti_{0.4}O_3$ are far off from those of known dielectrics in the McPherson curve, and there are no other dielectrics comparable to $BaHf_{0.6}Ti_{0.4}O_3$.

Field-effect transistors

Figure 3 shows an n-type accumulation mode FET using $BaHf_{0.6}Ti_{0.4}O_3$ as the gate oxide. Cross-sectional schematic diagram of the device is shown in Fig. 3A. First, to reduce the threading dislocation density, 150-nm-thick $BaSnO_3$ buffer layer was grown on a $SrTiO_3$ substrate. On top of it, 26-nm-thick 0.1% La-doped $BaSnO_3$ channel layer was grown using a micromachined silicon stencil mask

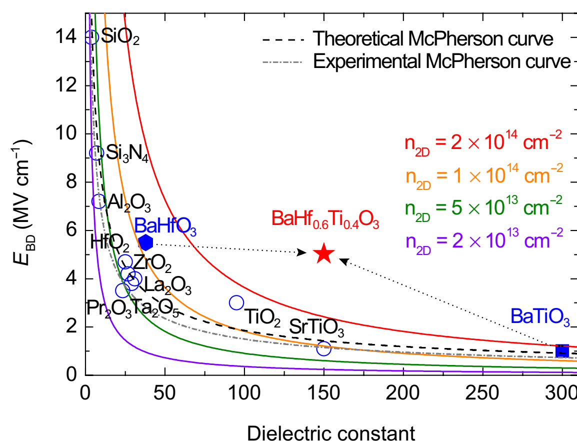

Fig. 2. Comparison of dielectric constant, breakdown field of dielectric materials including well-known high-*k* materials. Each colored lines denotes maximum field-induced charge densities. Black dashed lines and gray dashed-dotted lines are theoretical and experimental McPherson dielectric constant–breakdown field relations, respectively.

patterned as a line. A 4% La-doped $BaSnO_3$ was grown on it through a stainless steel mask as the source and the drain contacts, which defines the channel length. Last, using other Si masks, 100-nm-thick $BaHf_{0.6}Ti_{0.4}O_3$ gate oxide layer and 4% La-doped $BaSnO_3$ gate electrode were grown. Figure 3B shows the microscope image of the device. The channel width (W) of 0.1% La-doped $BaSnO_3$ is 140 μm, and the channel length (L) is 60 μm. More detailed geometry of the device is shown in fig. S6. The output characteristics of the device are shown in Fig. 3C. The source-drain voltage (V_{DS}) was applied up to 3 V, while the gate voltage (V_{GS}) was varied from 7 to 0 V with the interval of 1 V. At low V_{DS}, the drain current (I_D) is proportional to the V_{DS}, and as V_{DS} increases, I_D becomes saturated. The transfer characteristics of the device are shown in Fig. 3D. The gate leakage current (I_G) and I_D were measured at V_{DS} = 0.1 V, while V_{GS} was swept from 0 to 7 V. I_{on}/I_{off} ratio is about 10^7. The subthreshold swing value was evaluated from the relation $S = [\partial \log (I_D)/\partial V_{GS}]^{-1}$ as 0.14 V $decade^{-1}$. Field-effect mobility (μ_{FE}) of the device was calculated using the relation for the linear region

$$\mu_{FE,lin} = \frac{L}{W C_{ox} V_{DS}} \left(\frac{\partial I_D}{\partial V_{GS}} \right) = \frac{Lt}{W \kappa \varepsilon_0 V_{DS}} \left(\frac{\partial I_D}{\partial V_{GS}} \right) \quad (1)$$

where L, W, C_{ox}, t, and ε_0 are the channel length, the channel width, the capacitance per unit area of the $BaHf_{0.6}Ti_{0.4}O_3$ layer, the thickness of the $BaHf_{0.6}Ti_{0.4}O_3$ layer, and the permittivity of the vacuum, respectively. Threshold voltage of the device (V_T) is determined in the saturation region (V_{DS} = 5 V) by the linear $\sqrt{I_D}$ versus V_{GS} plot in fig. S7, which is 3.6 and 4.0 V for the increasing and the decreasing V_{GS}, respectively. The maximum of μ_{FE} is about 30 $cm^2\ V^{-1}\ s^{-1}$ when calculated by using average C_{ox} at low bias (k ~ 120 near 0.5 MV cm^{-1}). Compared to the FET with BHO gate oxide (*33*), although the La doping concentration is different, the V_{GS} required to modulate the current amplification of 10^7 (+3 to +7 V) is smaller (−7 to +18 V in case of BHO), which is attributed to the higher dielectric constant of $BaHf_{0.6}Ti_{0.4}O_3$ than BHO. The subthreshold swing value is also smaller than that of the BHO device (0.8 V $decade^{-1}$).

There were attempts to modulate the carrier density over 10^{14} cm^{-2} using solid-state oxides with very high dielectric constant, such as BTO and $SrTiO_3$ (*37*–*39*). Depletion-mode FETs using BTO as the gate dielectric were recently reported (*37*). However, the capability of the device to modulate the charge density was only 5.7×10^{13} cm^{-2}, and the off-state gate leakage current was 11.0 mA mm^{-1} at $V_g = -6$ V corresponding to 1.72×10^3 A cm^{-2} at −3 MV cm^{-1}, which is too high to be used in practical applications. There were $SrTiO_3$-based devices that modulated the carrier density over 1×10^{14} cm^{-2} (*38*, *39*). $SrTiO_3/GdTiO_3$ heterostructure FETs modulated the interfacial 2D electron gas of 1.1×10^{14} cm^{-2} (*38*). However, the device was not able to pinch off the channel completely. The other device is $SrTiO_3$-based Metal Semiconductor Field Effect Transistor, which modulated the charge density of 1.62×10^{14} cm^{-2} (*39*). Again, the off-state leakage current of the device was about 0.1 mA mm^{-1} at 1.875 MV cm^{-1}, which is also too high and probably responsible for the low on/off ratio of only 10^3, although the exact dimensions of the device are not presented.

To directly demonstrate the charge modulation larger than 10^{14} cm^{-2}, we fabricated n-type depletion-mode FETs using 33-nm-thick of 0.4% La-doped $BaSnO_3$ as the channel layer. The thickness of the BLSO channel layer was confirmed by an atomic force microscopy (AFM) thickness profile in fig. S8. Since 20-nm-thick 0.4% La-doped

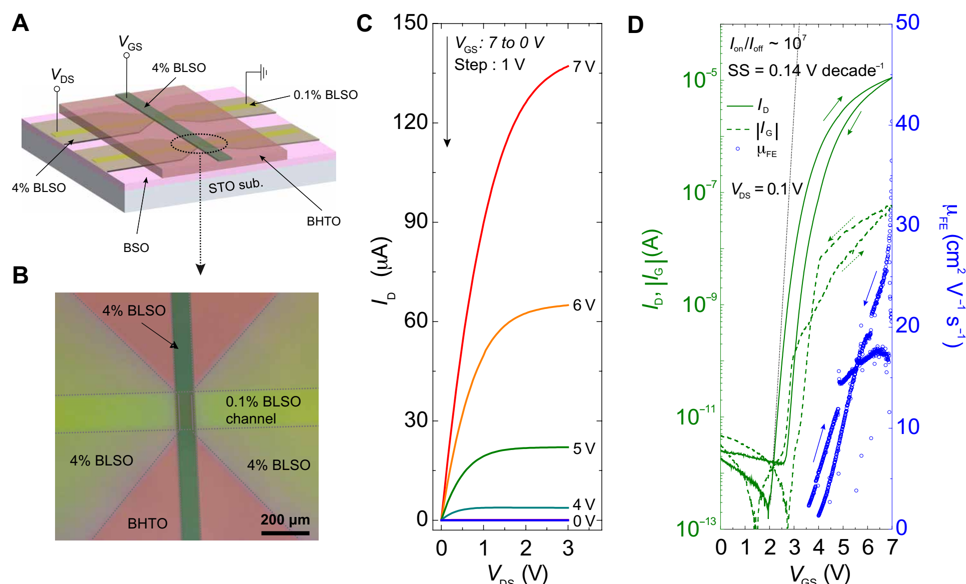

Fig. 3. FET in an n-type accumulation mode made with 0.1% BLSO channel layer and $BaHf_{0.6}Ti_{0.4}O_3$ gate oxide. (**A**) Schematic of the device. BSO, $BaSnO_3$. (**B**) The top view of the device pictured by an optical microscope. Gray dotted lines are plotted to illustrate each deposited layer. The channel width (W) of 0.1% La-doped $BaSnO_3$ is 140 μm, and the channel length (L) is 60 μm. (**C**) The output characteristic of the device. (**D**) Transfer characteristics of the device. Source-drain current is plotted in a full green line, and leakage current is plotted in a dashed green line. Calculated field-effect mobility is shown in blue circle scatter plot. Black dashed line shows the maximum subthreshold swing (SS) of the device.

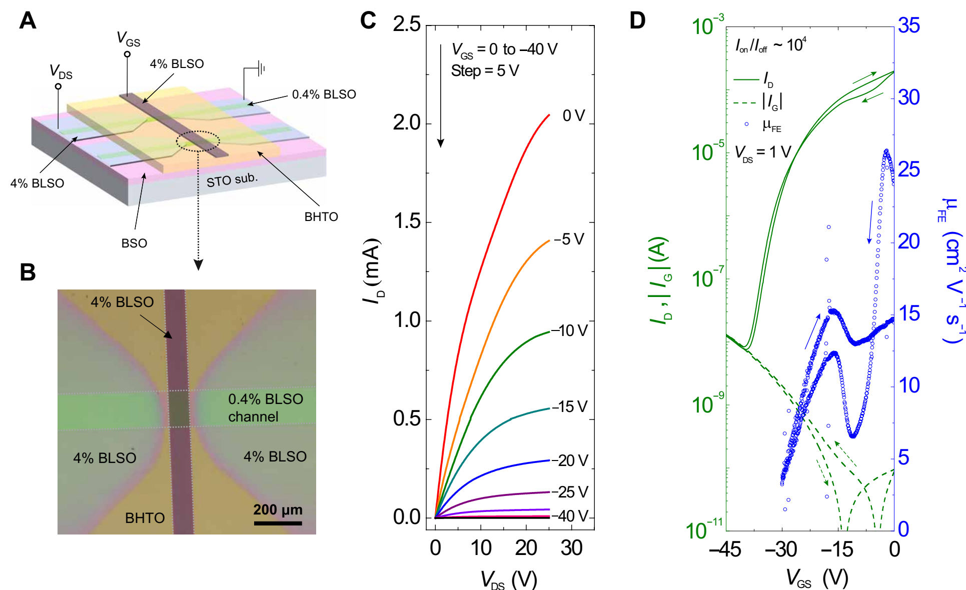

Fig. 4. FET in an n-type depletion mode made with 0.4% La-doped $BaSnO_3$ channel layer and $Hf_{0.6}Ti_{0.4}O_3$ gate oxide. (**A**) Schematic of the device. (**B**) The top view of the device pictured by an optical microscope. Gray dotted lines are plotted to illustrate each deposited layer. The channel width (W) of 0.4% La-doped $BaSnO_3$ is 140 μm, and the average channel length (L) is 130 μm. (**C**) The output characteristic of the device. (**D**) Transfer characteristics of the device. Source-drain current is plotted in a full green line, and leakage current is plotted in a dashed green line. Calculated field-effect mobility is shown in blue circle scatter plot.

$BaSnO_3$ films was found to have a 2D carrier density of 7.03×10^{13} cm^{-2} by a separate Hall measurement in fig. S9, the channel of 33 nm in thickness is estimated to have $n_{2D} = 1.16 \times 10^{14}$ cm^{-2}. The cross-sectional schematic of the device is shown in Fig. 4A. To define the channel width, a 140-μm-width silicon stencil mask was used. After deposition of the buffer and the channel layers, 4% La-doped $BaSnO_3$ channel contact layer was deposited using a stainless steel mask, which defines the average of 130 μm in channel length. On top of it, 200-nm-thick $BaHf_{0.6}Ti_{0.4}O_3$ gate oxide was deposited using a silicon stencil mask. To define the gate length of 80 μm, we deposited 4% La-doped $BaSnO_3$ gate electrode layer using a silicon stencil mask. The detailed geometry of the device is shown in fig. S10. Figure 4B shows the microscope image of the device. The output characteristic of the device is shown in Fig. 4C. The V_{DS}

was applied up to 25 V, while the V_{GS} was varied from 0 to −40 V with the interval of 5 V. At low V_{DS}, the I_D is proportional to the V_{DS}, and as V_{DS} increases, I_D becomes saturated, which is a characteristic of a typical n-type FET. The transfer characteristics of the device are shown in Fig. 4D. I_G and I_D were measured at V_{DS} = 1 V, while V_{GS} was swept from 0 to −45 V. I_{on}/I_{off} ratio is about 10^4, limited by relatively high off-state I_D due to the high I_G. The field-effect mobility (μ_{FE}) of the device was calculated using Eq. 1. The C_{ox} in the device was measured, as shown in fig. S11, and used for the calculation. The maximum of μ_{FE} is about 15 to 25 cm^2 V^{-1} s^{-1}. The channel of 0.4% La-doped $BaSnO_3$ was depleted until I_D is limited by I_G. Using the leakage current density of 10^{-4} A cm^{-2} at 2 MV cm^{-1} in Fig. 1, when the device is scaled down to 0.1 μm in channel length and 10 μm in channel width, the leakage current will decrease to 10^{-12} A at 2 MV cm^{-1}, which would satisfy the requirements of field-effect devices of on-current of larger than 1 mA μm^{-1} and off-current of 10^{-12} A. Direct modulation of carrier density over 10^{14} cm^{-2} was realized using solid-state gate oxide, which has not been realized to date. The *C-V* measurement of the device in fig. S11 confirms the modulation of 1.07×10^{14} cm^{-2}.

Structural properties and compositional modulation

Figure S12A is the high-angle annular dark field-scanning transmission electron microscope (HAADF-STEM) image with various scales, and fig. S12B is the low-angle annular dark-field scanning transmission electron microscope (LAADF-STEM) image of $BaHf_{0.6}Ti_{0.4}O_3$ on the identical region of film. In LAADF-STEM image, which is more sensitive to the local strain (*40*), there is evident contrast of

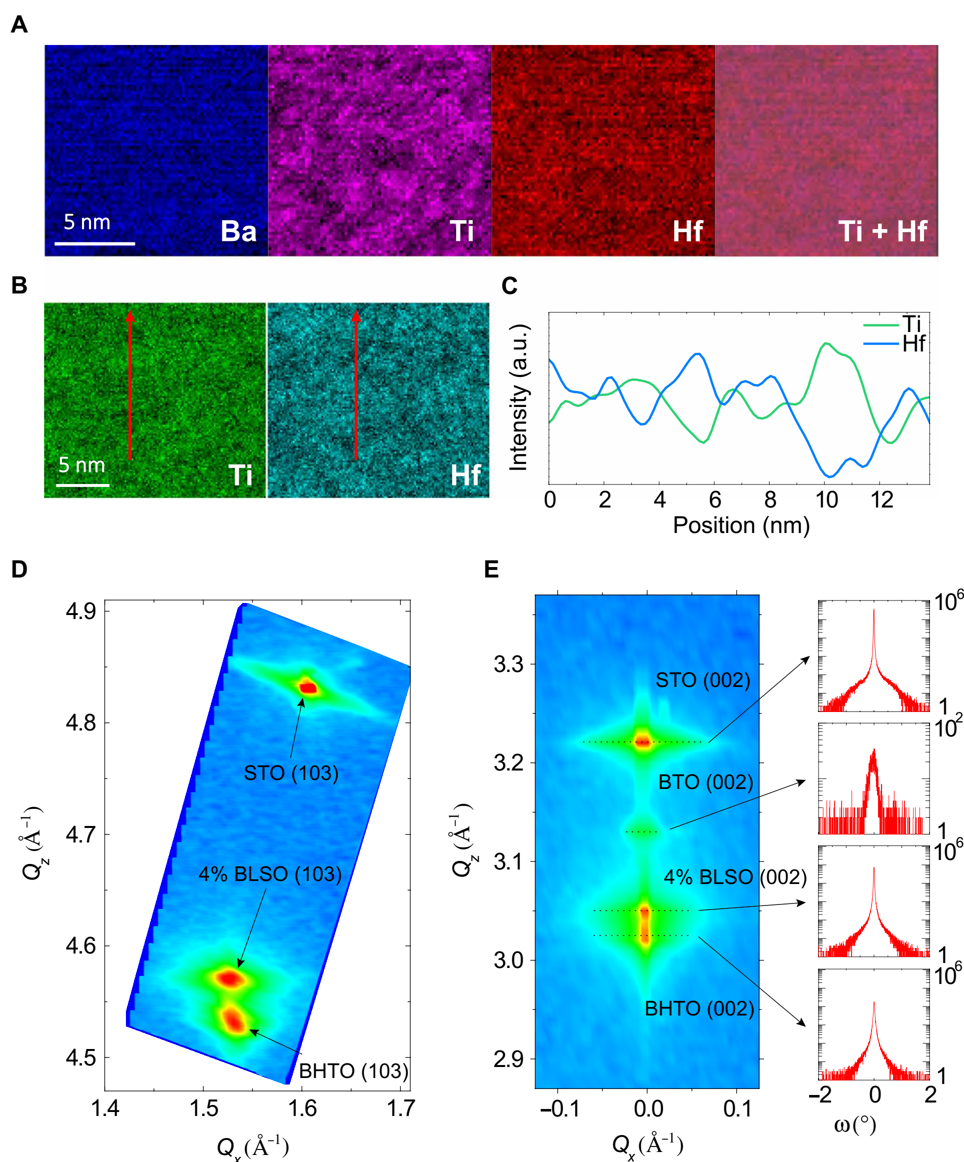

Fig. 5. Structural properties of BHTO. (**A**) EELS element mapping image of $BaHf_{0.6}Ti_{0.4}O_3$. (**B**) Region of EELS line scan. Red arrows denote scan directions. (**C**) Line profile of Ti and Hf elements. a.u., arbitray units. (**D**) RSM of $BaHf_{0.6}Ti_{0.4}O_3$ (103) peak. (**E**) (002) peaks and corresponding rocking curves. Black dashed lines are rocking curve scan regions. Detailed rocking curves and FWHM are presented in fig. S13.

atoms when compared to HAADF-STEM image of $BaHf_{0.6}Ti_{0.4}O_3$. The bright side of the image is presumed to be Ti-rich region. To confirm the stoichiometric modulation, we measured the electron energy-loss spectroscopy (EELS) of the film to distinguish the atomic configuration of the $BaHf_{0.6}Ti_{0.4}O_3$ film, as shown in Fig. 5A. In Ti mapping, the configuration of Ti atoms is similar to the LAADF-STEM image, which suggests Ti-rich clustering in 2-nm scale. The Hf distribution complements that of the Ti distribution, since the overlapped mapping image of Ti and Hf together generates images very similar to that of Ba, which is homogeneous throughout. Figure 5 (B and C) is the EELS line scan profiles, which confirms the chemical heterogeneity of Hf and Ti atoms. The intensities for the two atoms in line scan profiles are complementary, as expected in a chemically modulated system. To further confirm the chemical heterogeneity of Hf and Ti atoms, we measured the structural property of $BaHf_{0.6}Ti_{0.4}O_3$ by x-ray diffraction measurement. A degenerately doped 4% La-doped $BaSnO_3$ layer was grown first as the bottom electrode on $SrTiO_3$ substrates. $BaHf_{0.6}Ti_{0.4}O_3$ layer (~200 nm in thickness) was epitaxially grown on top of it. Reciprocal space mapping (RSM) measurements were performed on the $BaHf_{0.6}Ti_{0.4}O_3$ (103) and (002) peaks, as shown in Fig. 5 (D and E). In $BaHf_{0.6}Ti_{0.4}O_3$ (103) peak in Fig. 5D, corresponding in-plane and out-of-plane lattice parameters, a and c, are 4.096 and 4.158 Å, respectively. Considering the cubic BHO bulk lattice parameter of a = 4.171 Å and the tetragonal BTO bulk lattice parameters of a = 4.000 Å and c = 4.022 Å, the in-plane lattice value is close to an expectation, although it does not seem to be pinned with that of the underlying La-doped $BaSnO_3$. The in-plane and out-of-plane lattice parameters indicate that the $BaHf_{0.6}Ti_{0.4}O_3$ film is grown as tetragonal structure, which can contribute to the large dielectric constant. In RSM of (002) peaks shown in Fig. 5E, a tiny but isolated BTO peak with corresponding out-of-plane lattice parameter of c = 4.013 Å is measured, which is a direct evidence of clustering of Ti-rich region. However, no BHO peaks were observed. Detailed rocking curves of the film are shown in fig. S13. Full widths at half maximum (FWHMs) are 0.028 and 0.036 for the 4% BLSO layer and the $BaHf_{0.6}Ti_{0.4}O_3$ layer, respectively, which is close to that of the $SrTiO_3$ single-crystal substrate, 0.023, while FWHM of the BTO peak is 0.286. Thus, only the BTO peak has much broader FWHM, not coherent with other peaks, which indicates nanoscale clustering of the material. This can explain the absence of pinning of the in-plane lattice constant despite less than 0.5% mismatch in the average lattice constants of La-doped $BaSnO_3$ and $BaHf_{0.6}Ti_{0.4}O_3$.

Figure S14 shows optical absorption measurement to measure the optical bandgap. The optical bandgap of $BaHf_{0.6}Ti_{0.4}O_3$ was measured to be 4.4 eV. Such a bandgap can support the measured dielectric breakdown field of 5.0 MV cm^{-1} when one assumes that the breakdown field is indeed limited by the bandgap (*41*). However, in most practical cases, defect states exist inside the bandgap, which work as leakage current paths and lower the breakdown field.

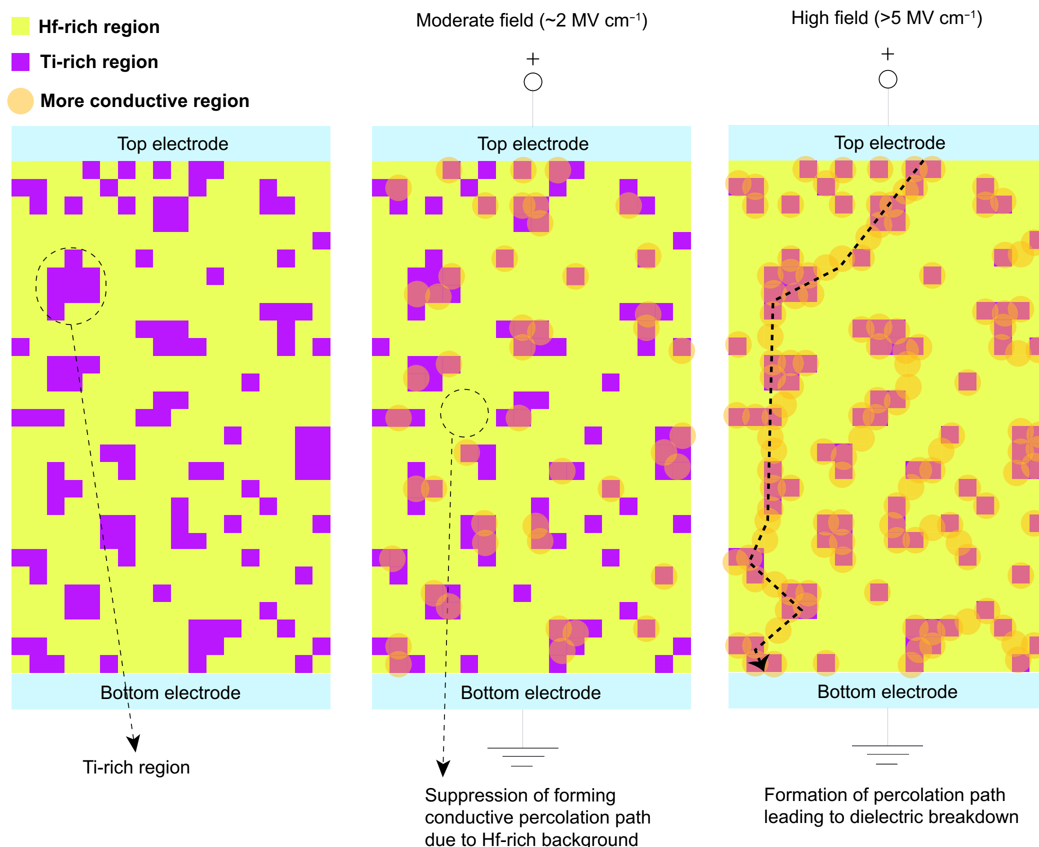

Fig. 6. Percolation path formation model in heterogeneous $BaHf_{0.6}Ti_{0.4}O_3$ system. In Ti-rich regions, defects are more easily generated compared to Hf-rich regions when electric field is applied, forming the conductive regions. Continuous overlap of conductive region results in formation of a percolating path, lastly leading to a large leakage current and the dielectric breakdown, which involves irreversible damage to the dielectric layer.

The reason why $BaHf_{0.6}Ti_{0.4}O_3$ dielectric has both high dielectric constant and high breakdown field with a moderately high bandgap is attributed to the following. High dielectric strength background material (Hf-rich) with inclusion of high dielectric constant material (Ti-rich) has a large average polarization in applied external electric field, resulting in high dielectric constant. At the same time, the high dielectric strength background prevents a conductive percolation path from forming, which leads to low leakage current and large breakdown field. Therefore, proper combination of materials with high dielectric strength and high dielectric constant materials can optimize both electric properties, as visualized in Fig. 6.

We investigated the dielectric properties of $BaHf_{0.6}Ti_{0.4}O_3$, which is an alloy of large dielectric strength material and the high dielectric constant material. We found that carrier density of larger than 10^{14} cm^{-2} can be modulated through $BaHf_{0.6}Ti_{0.4}O_3$ dielectric. The key to excellent dielectric properties is the nanometer scale stoichiometric modulation of high large dielectric strength material background and high dielectric constant material inclusion. We demonstrate the n-type accumulation mode and n-type depletion-mode FETs using $BaHf_{0.6}Ti_{0.4}O_3$ gate oxide with excellent FET characteristics, which has been unattainable via other conventional dielectrics.

MATERIALS AND METHODS

Raw materials

All material targets of $BaSnO_3$, La-doped $BaSnO_3$, and $BaHf_{0.6}Ti_{0.4}O_3$ (BHTO) were provided by Toshima Manufacturing Co. in Japan, which have a purity over 99.9%.

Thin film growth

All BHTO samples were grown on $SrTiO_3$ or MgO single-crystal substrates at 750°C in oxygen partial pressure of 10 mtorr by pulsed laser deposition system. KrF excimer laser with 248-nm wavelength was used with energy fluence of about 1.2 to 1.5 J cm^{-2} and a repetition rate at 10 Hz. For BHTO, the distance between the target and the substrate is 63 mm. La-doped $BaSnO_3$ layers were deposited in oxygen partial pressure of 100 mtorr at 750°C with the distance between the target and the substrate of 54 or 58.5 mm and used as the electrode and the channel layer respectively. To make lateral patterns, Si or stainless steel stencil masks were used. The thicknesses of films are confirmed by stylus profiler (DektakXT-E, Bruker) or AFM (LensAFM, Nanosurf).

Structural characterizations

The high quality of the films was confirmed by D8 DISCOVER high-resolution diffractometer (Bruker), operated at 40 kV and 60 mA with Cu K_α (λ = 1.5406 Å) radiation. (Fig. 5 and figs. S1 and S13).

Transport measurement

Electrical properties were measured using the Keithley 4200 semiconductor characterization system. We obtained the parallel capacitance (C_p) and dissipation factor (tan δ) from the admittance measurement with an AC voltage of 30 mV and the root mean square amplitude applied. For the breakdown field (E_{BD}) measurement, the leakage current through the capacitors was measured with voltage sweep measurement.

Bandgap measurement

We measured the optical absorption of samples by using a grating spectrometer (Cary 5000, Bruker) over 200 to 2000 nm (0.6 to 6.2 eV). The spectrometer has a quartz iodine lamp light source for 2000 to 350 nm, and a deuterium untraviolet lamp light source for below 350 nm. Samples are mounted on a holder with a 3-mm-diameter hole. Absorbance is calculated as the minus logarithm of the transmittance, and absorption coefficient α is calculated by accounting for the sample thickness. About 200-nm-thick $BaHf_{0.6}Ti_{0.4}O_3$ layer was grown on MgO substrate (E_g ~ 8 eV) to prevent absorption by the substrate. We removed the substrate absorption by measuring the MgO substrate's optical absorption separately and subtracting the absorbance of the two samples. From the optical absorption measurement, we plotted the Tauc's plot of $(\alpha\hbar\omega)^2$ versus ($\hbar\omega$), where α denotes absorption coefficient, assuming a direct bandgap (fig. S14).

STEM and EELS analysis

The sample of the BHTO films, oriented in the [100] direction, for cross-sectional imaging was prepared by the Ga ion beam milling using focused ion beam (Thermo Fisher Scientific, Helios 5 HX) at an acceleration voltage of 15 kV. A further 1-kV Ga ion beam milling was conducted to eliminate the surface damages of the sample. STEM and EELS analyses were performed on an aberration-corrected STEM (Thermo Fisher Scientific, Titan Cubed 60-300) equipped with EELS (Gatan, Quantum ERS 966), operating at 300 kV with a semiconvergence angle of 26.5 mrad. The HAADF/LAADF STEM images were acquired with detector angles ranging from 40 to 200 and 25 to 47 mrad, respectively. EELS spectrum imaging was recorded with the energy range of 200 to 2248 eV to detect the Ti-$L_{2,3}$, O-K, Ba-$M_{4,5}$, and Hf-$M_{4,5}$ with an energy resolution of ~0.9 eV. The dwell time per pixel and the dispersion were 0.02 s and 1 eV/ch, respectively.

SUPPLEMENTARY MATERIALS

Supplementary material for this article is available at https://science.org/doi/10.1126/sciadv.abm3962

REFERENCES AND NOTES

1. S. Salahuddin, K. Ni, S. Datta, The era of hyper-scaling in electronics. *Nat. Electron.* **1**, 442–450 (2018).
2. G. D. Wilk, R. M. Wallace, J. M. Anthony, High-κ gate dielectrics: Current status and materials properties considerations. *J. Appl. Phys.* **89**, 5243–5275 (2001).
3. J. Robertson, R. M. Wallace, High-K materials and metal gates for CMOS applications. *Mater. Sci. Eng. R Rep.* **88**, 1–41 (2015).
4. R. Droopad, Z. Yu, J. Ramdani, L. Hilt, J. Curless, C. Overgaard, J. L. Edwards Jr., J. Finder, K. Eisenbeiser, W. Ooms, Development of high dielectric constant epitaxial oxides on silicon by molecular beam epitaxy. *Mater. Sci. Eng. B* **87**, 292–296 (2001).
5. J. McPherson, J. Kim, A. Shanware, H. Mogul, J. Rodriguez, Proposed universal relationship between dielectric breakdown and dielectric constant. *IEEE Dig. Int. Electron Devices Meet.* , 633–636 (2002).
6. S. Z. Bisri, S. Shimizu, M. Nakano, Y. Iwasa, Endeavor of iontronics: From fundamentals to applications of ion-controlled electronics. *Adv. Mater.* **29**, 1607054 (2017).
7. H. Yuan, H. Shimotani, A. Tsukazaki, A. Ohtomo, M. Kawasaki, Y. Iwasa, High-density carrier accumulation in ZnO field-effect transistors gated by electric double layers of ionic liquids. *Adv. Funct. Mater.* **19**, 1046–1053 (2009).
8. K. Fujiwara, K. Nishihara, J. Shiogai, A. Tsukazaki, Enhanced electron mobility at the two-dimensional metallic surface of $BaSnO_3$ electric-double-layer transistor at low temperatures. *Appl. Phys. Lett.* **110**, 203503 (2017).
9. J. McPherson, J.-Y. Kim, A. Shanware, H. Mogul, Thermochemical description of dielectric breakdown in high dielectric constant materials. *Appl. Phys. Lett.* **82**, 2121–2123 (2003).
10. J. W. McPherson, J. Kim, A. Shanware, H. Mogul, J. Rodriguez, Trends in the ultimate breakdown strength of high dielectric-constant materials. *IEEE Trans. Electron Devices* **50**, 1771–1778 (2003).
11. J. J. Kim, M. Kim, U. Jung, K. E. Chang, S. Lee, Y. Kim, Y. G. Lee, R. Choi, B. H. Lee, Intrinsic time zero dielectric breakdown characteristics of HfAlO alloys. *IEEE Trans. Electron Devices* **60**, 3683–3689 (2013).

12. L.-M. Wang, Relationship between intrinsic breakdown field and bandgap of materials, in *2006 25th International Conference on Microelectronics* (IEEE, 2006), pp. 576–579.
13. R. A. McKee, F. J. Walker, M. F. Chisholm, Crystalline oxides on silicon: The first five monolayers. *Phys. Rev. Lett.* **81**, 3014–3017 (1998).
14. K. Eisenbelser, J. M. Finder, Z. Yu, J. Ramadani, J. A. Curless, J. A. Hallmark, R. Droopad, W. J. Ooms, L. Salem, S. Bradshaw, C. D. Overgaard, Field effect transistors with $SrTiO_3$ gate dielectric on Si. *Appl. Phys. Lett.* **76**, 1324–1326 (2000).
15. C. J. Forst, C. R. Ashman, K. Schwarz, P. E. Blochl, The interface between silicon and a high-k oxide. *Nature* **427**, 53–56 (2004).
16. C. Rossel, B. Mereu, C. Marchiori, D. Caimi, M. Sousa, A. Guiller, H. Siegwart, R. Germann, J.-P. Locquet, J. Fompeyrine, D. J. Webb, C. Dieker, J. W. Seo, Field-effect transistors with $SrHfO_3$ as gate oxide. *Appl. Phys. Lett.* **89**, 053506 (2006).
17. C. Rossel, M. Sousa, C. Marchiori, J. Fompeyrine, D. Webb, D. Caimi, B. Mereu, A. Ispas, J. P. Locquet, H. Siegwart, R. Germann, A. Tapponnier, K. Babich, $SrHfO_3$ as gate dielectric for future CMOS technology. *Microelectron. Eng.* **84**, 1869–1873 (2007).
18. T. Q. Ngo, A. B. Posadas, M. D. McDaniel, C. Hu, J. Bruley, E. T. Yu, A. A. Demkov, J. G. Ekerdt, Epitaxial c-axis oriented $BaTiO_3$ thin films on SrTiO3-buffered Si(001) by atomic layer deposition. *Appl. Phys. Lett.* **104**, 082910 (2014).
19. D. Pierangeli, M. Ferraro, D. Mei, G. D. Domenico, C. E. M. de Oliveira, A. J. Agranat, E. DelRe, Super-crystals in composite ferroelectrics. *Nat. Commun.* **7**, 10674 (2016).
20. V. A. Stoica, N. Laanait, C. Dai, Z. Hong, Y. Yuan, Z. Zhang, S. Lei, M. R. McCarter, A. Yadav, A. R. Damodaran, S. Das, G. A. Stone, J. Karapetrova, D. A. Walko, X. Zhang, L. W. Martin, R. Ramesh, L.-Q. Chen, H. Wen, V. Gopalan, J. W. Freeland, Optical creation of a supercrystal with three-dimensional nanoscale periodicity. *Nat. Mater.* **18**, 377–383 (2019).
21. M. Hadjimichael, Y. Li, E. Zatterin, G. A. Chahine, M. Conroy, K. Moore, E. N. O' Connell, P. Ondrejkovic, P. Marton, J. Hlinka, U. Bangert, S. Leake, P. Zubko, Metal-ferroelectric supercrystals with periodically curved metallic layers. *Nat. Mater.* **20**, 495–502 (2021).
22. X. Gao, Z. Cheng, Z. Chen, Y. Liu, X. Meng, X. Zhang, J. Wang, Q. Guo, B. Li, H. Sun, Q. Gu, H. Hao, Q. Shen, J. Wu, X. Liao, S. P. Ringer, H. Liu, L. Zhang, W. Chen, F. Li, S. Zhang, The mechanism for the enhanced piezoelectricity in multi-elements doped $(K,Na)NbO_3$ ceramics. *Nat. Commun.* **12**, 881 (2021).
23. Y. M. Kim, C. Park, T. Ha, U. Kim, N. Kim, J. Shin, Y. Kim, J. Yu, J. H. Kim, K. Char, High-k perovskite gate oxide $BaHfO_3$. *APL Mater.* **5**, 016104 (2017).
24. M. B. Smith, K. Page, T. Siegrist, P. L. Redmond, E. C. Walter, R. Seshadri, L. E. Brus, M. L. Steigerwald, Crystal structure and the paraelectric-to-ferroelectric phase transition of nanoscale $BaTiO_3$. *J. Am. Chem. Soc.* **130**, 6955–6963 (2008).
25. R. Thomas, D. C. Dube, M. N. Kamalasanan, S. Chandra, Optical and electrical properties of $BaTiO_3$ thin films prepared by chemical solution deposition. *Thin Solid Films* **346**, 212–225 (1999).
26. Q. X. Jia, Z. Q. Shi, W. A. Anderson, $BaTiO_3$ thin film capacitors deposited by r.f. magnetron sputtering. *Thin Solid Fim* **209**, 230–239 (1992).
27. S. Cho, C. Yun, Y. S. Kim, H. Wang, J. Jian, W. Zhang, J. Huang, X. Wang, H. Wang, J. L. M-Driscoll, Strongly enhanced dielectric and energy storage properties in lead-free perovskite titanate thin films by alloying. *Nano Energy* **45**, 398–406 (2018).
28. S. Halder, T. Schneller, R. Waser, S. B. Majumder, Electrical and optical properties of chemical solution deposited barium hafnate titanate thin films. *Thin Solid Films* **516**, 4970–4976 (2008).
29. H. Y. Tian, Y. Wang, J. Miao, H. L. W. Chan, C. L. Choy, Preparation and characterization of hafnium doped barium titanate ceramics. *J. Alloys Compd.* **431**, 197–202 (2007).
30. G. Lupina, O. Seifarth, G. Kozlowski, P. Dudek, J. Dabrowski, G. Lippert, H.-J. Mussig, Hf- and Zr-based alkaline earth perovskite dielectrics for memory applications. *Microelectron. Eng.* **86**, 1842–1844 (2009).
31. A. Abrutis, T. Katkus, S. Stanionytė, V. Kubilius, G. Lupina, C. Wenger, M. Lukosius, Chemical vapor deposition and characterization of high-k $BaHf_{1-x}Ti_xO_3$ dielectric layers for microelectronic applications. *J. Vac. Sci. Technol. B* **29**, 01A303 (2011).
32. P. Dudek, G. Lupina, G. Kozłowski, P. Zaumseil, J. Bauer, O. Fursenko, J. Dabrowski, R. Schmidt, G. Lippert, H.-J. Müssig, T. Schroeder, D. Schmeißer, E. Zschech, Atomic-scale engineering of future high-*k* dynamic random access memory dielectrics: The example of partial Hf substitution by Ti in $BaHfO_3$. *J. Vac. Sci. Technol. B* **29**, 01AC03 (2011).
33. H. J. Kim, U. Kim, H. M. Kim, T. H. Kim, H. S. Mun, B. G. Jeon, K. T. Hong, W. J. Lee, C. Ju, K. H. Kim, K. Char, High mobility in a stable transparent perovskite oxide. *Appl. Phys. Express* **5**, 061102 (2012).
34. K. Abe, S. Komatsu, Dielectric constant and leakage current of epitaxially grown and polycrystalline $SrTiO_3$ thin films. *Jpn. J. Appl. Phys.* **32**, 4186–4189 (1993).
35. P. A. Fleury, J. M. Worlock, Electric-field induced Raman scattering in $SrTiO_3$ and $KTaO_3$. *Phys. Rev.* **174**, 613–623 (1968).
36. I. A. Akimov, A. A. Sirenko, A. M. Clark, J.-H. Hao, X. X. Xi, Electric-field induced soft-mode hardening in $SrTiO_3$ films. *Phys. Rev. Lett.* **84**, 4625–4628 (2000).
37. J. Cheng, C. Wang, C. Freeze, O. Shoron, N. Combs, H. Yang, N. K. Kalarickal, Z. Xia, S. Stemmer, S. Rajan, W. Lu, High-current perovskite oxide $BaTiO_3/BaSnO_3$ heterostructure field effect transistors. *IEEE Electron Device Lett.* **41**, 621–624 (2020).
38. M. Boucherit, O. Shoron, C. A. Jackson, T. A. Cain, M. L. C. Buffon, C. Polchinski, S. Stemmer, S. Rajan, Modulation of over 10^{14} cm^{-2} electrons in $SrTiO_3/GdTiO_3$ heterostructures. *Appl. Phys. Lett.* **104**, 182904 (2014).
39. A. Verma, S. Raghavan, S. Stemmer, D. Jena, Au-gated $SrTiO_3$ field-effect transistors with large electron concentration and current modulation. *Appl. Phys. Lett.* **105**, 113512 (2014).
40. D. A. Muller, N. Nakagawa, A. Ohtomo, J. L. Grazul, H. Y. Hwang, Atomic-scale imaging of nanoengineered oxygen vacancy profiles in $SrTiO_3$. *Nature* **430**, 657–661 (2004).
41. M. Higashiwaki, K. Sasaki, A. Kuramata, T. Masui, S. Yamakoshi, Gallium oxide (Ga_2O_3) metal-semiconductor field-effect transistors on single-crystal β-Ga_2O_3 (010) substrates. *Appl. Phys. Lett.* **100**, 013504 (2012).
42. V. Lucarini, J. J. Saarinen, K.-E. Peiponen, E. M. Vartianinen, in *Kramer-Kronig Relations in Optical Materials Research* (Springer, 2005), pp. 11–26.
43. M. Kadoshima, M. Hiratani, Y. Shimamoto, K. Torii, H. Miki, S. Kimura, T. Nabatame, Rutile-type TiO_2 thin film for high-k gate insulator. *Thin Solid Films* **424**, 224–228 (2003).
44. M. Shin, M. R. D. Guire, A. H. Heuer, Electrical properties of TiO_2 thin films formed on self-assembled organic monolayers on silicon. *J. Appl. Phys.* **83**, 3311–3317 (1998).
45. M.-K. Lee, C.-F. Yen, Comprehension of postmetallization annealed MOCVD-TiO_2 on $(NH_4)_2S$ treated III-V semiconductors. *Act. Passiv. Electron. Compon.* **2012**, 148705 (2012).
46. J. H. Choi, Y. Mao, J. P. Chang, Development of hafnium based high-*k* materials—A review. *Mater. Sci. Eng. R Rep.* **72**, 97–136 (2011).
47. V. A. Shvets, V. S. Aliev, D. V. Gritsenko, S. S. Shaimeev, E. V. Fedosenko, S. V. Rykhlitski, V. V. Atuchin, V. A. Gritsenko, V. M. Tapilin, H. Wong, Electronic structure and charge transport properties of amorphous Ta_2O_5 films. *J. Non Cryst. Solids* **354**, 3025–3033 (2008).
48. J.-L. Autran, R. Devine, C. Chaneliere, B. Bernard, Fabrication and characterization of Si-MOSFET's with PECVD amorphous Ta_2O_5 gate insulator. *IEEE Electron Device Lett.* **18**, 447–449 (1997).
49. B. H. Lee, L. Kang, W.-J. Qi, R. Nieh, Y. Jeon, K. Onishi, J. C. Lee, Ultrathin hafnium oxide with low leakage and excellent reliability for alternative gate dielectric application, in *Proceedings of the IEEE Technical Digest. International Electron Devices Meeting* (IEEE, 1999), pp. 133–136.
50. C. M. Perkins, B. B. Triplett, P. C. McIntyre, K. C. Saraswat, S. Haukka, M. Tuominen, Electrical and materials properties of ZrO_2 gate dielectrics grown by atomic layer chemical vapor deposition. *Appl. Phys. Lett.* **78**, 2357–2359 (2001).
51. J. Chen, T. Kawanago, H. Wakabayashi, K. Tsutsui, H. Iwai, D. Nohata, H. Nohira, K. Kakushima, La_2O_3 gate dielectrics for AlGaN/GaN HEMT. *Microelectron. Reliab.* **60**, 16–19 (2016).
52. J. H. Shim, H. J. Choi, Y. Kim, J. Torgersen, J. An, M. H. Lee, F. B. Prinz, Process-property relationship in high-k ALD $SrTiO_3$ and $BaTiO_3$: A review. *J. Mater. Chem. C* **5**, 8000–8013 (2017).
53. M. D. McDaniel, C. Hu, S. Lu, T. Q. Ngo, A. Posadas, A. Jiang, D. J. Smith, E. T. Yu, A. A. Demkov, J. G. Ekerdt, Atomic layer deposition of crystalline $SrHfO_3$ directly on Ge (001) for high-k dielectric applications. *J. Appl. Phys.* **117**, 054101 (2015).
54. G. Lupina, G. Kozlowski, J. Dabrowski, P. Dudek, G. Lippert, H.-J. Mussig, Dielectric and structural properties of thin $SrHfO_3$ layers on TiN. *Appl. Phys. Lett.* **93**, 252907 (2008).
55. A. Feteira, D. C. Sinclair, K. Z. Rajab, M. T. Lanagan, Crystal structure and microwave dielectric properties of alkaline-earth hafnates, $AHfO_3$ (A=Ba, Sr, Ca). *J. Am. Ceram. Soc.* **91**, 893–901 (2008).

Acknowledgment: Part of this study has been performed using the facilities at IBS Center for Correlated Electron Systems, Seoul National University. **Funding:** This work is partially supported by the Samsung Electronics Co. Ltd. (project no. 0409-20200273). The work at Yonsei University was supported by the SRC program (vdWMRC; grant number 2017R1A5A1014862). **Author contributions:** K.C. conceived the original idea for the project. D.S. performed device fabrication and electrical measurements. The STEM measurements were performed by M.J. under the direction of K.L. and Y.K. The high-resolution x-ray diffraction measurements were performed by J.K. under the direction of B.K. Optical measurements were performed by Jae Ha Kim under the direction of Jae Hoon Kim. The manuscript was written by D.S. and K.C. with inputs from the other authors. All the works were supervised by K.C. All authors contributed to the scientific planning and discussions. **Competing interests:** The authors declare that they have no competing interests. **Data and materials availability:** All data needed to evaluate the conclusions of this study are present in the paper and/or the Supplementary Materials.

Submitted 14 September 2021
Accepted 27 January 2022
Published 18 March 2022
10.1126/sciadv.abm3962